Localization of microscale devices in vivo using addressable transmitters operated as magnetic spins

Manuel Monge[1], Audrey Lee-Gosselin[2], Mikhail G. Shapiro[2]* and Azita Emami[1]*

The function of miniature wireless medical devices, such as capsule endoscopes, biosensors and drug-delivery systems, depends critically on their location inside the body. However, existing electromagnetic, acoustic and imaging-based methods for localizing and communicating with such devices suffer from limitations arising from physical tissue properties or from the performance of the imaging modality. Here, we embody the principles of nuclear magnetic resonance in a silicon integrated-circuit approach for microscale device localization. Analogous to the behaviour of nuclear spins, the engineered miniaturized radio frequency transmitters encode their location in space by shifting their output frequency in proportion to the local magnetic field; applied field gradients thus allow each device to be located precisely from its signal's frequency. The devices are integrated in circuits smaller than 0.7 mm³ and manufactured through a standard complementary-metal-oxide-semiconductor process, and are capable of sub-millimetre localization in vitro and in vivo. The technology is inherently robust to tissue properties, scalable to multiple devices, and suitable for the development of microscale devices to monitor and treat disease.

The miniaturization of medical devices has enabled the development of new approaches for the diagnosis and treatment of human diseases[1,2]. For instance, smart pills are being used to image the gastrointestinal tract[3–5], distributed sensors are being developed to map the function of the brain[6,7], and microscale robots are being designed to access organs through the bloodstream[8]. Although substantial progress has been made in endowing microscale devices with the capability of sensing their environment, performing biopsies and releasing drugs[1,4,9,10], a major challenge remains in the way these devices communicate with the outside world.

Existing technologies are limited in their ability to precisely determine the location of microscale devices inside the body and communicate with them in a location-specific manner. For example, current techniques based on radio frequency (RF) signals[9,11–15] are limited in their resolution and ability to localize multiple devices due to the strong dependence of signal propagation on tissue properties and the close proximity of triangulating RF receivers to the implant. Meanwhile, approaches based on direct detection of magnetic fields generated by devices bearing permanent magnets or coils have a limited detection range[11], involve millimetre-sized architectures[16–23], and have not been applied at the microscale. Alternatively, device imaging using methods such as X-ray computed tomography[24–26], positron emission tomography[27], magnetic resonance imaging (MRI)[11,27–30] and ultrasound[9,11,27,31–34] are limited by the properties of each modality—such as the presence of background contrast or the use of ionizing radiation—with limited opportunity for information transfer to and from the device.

Here, we present an alternative approach to microscale device localization based on concepts from nuclear magnetic resonance. In particular, the magnetic-field-dependent precession frequency of nuclear spins allows their location in space to be encoded through the application of magnetic field gradients. This allows MRI to visualize signals from nuclear spins located throughout a specimen with

~100 μm resolution. We hypothesized that, by designing microscale devices whose output frequency could shift with the magnetic field, they too could be localized, read out and controlled with MRI-like precision. This would enable the development of indigestible or injectable sensors and actuators whose locations in the body could be pinpointed while they provide a readout of local physiological variables such as pH, pressure, temperature, electrical potential or concentration of certain analytes, or execute interventions such as releasing drugs, applying electrical stimulation or ablating tissue. Critically, multiple devices such as this distributed throughout the body or tissue could be addressed simultaneously. To test this concept, we developed a prototype device using a standard complementary metal-oxide-semiconductor (CMOS) process. Because it operates analogously to magnetic spins, we call this technology addressable transmitters operated as magnetic spins (ATOMS). We characterize the behaviour of ATOMS in 1D and 2D localization experiments, achieving sub-millimetre resolution. Finally, we demonstrate its potential for accurate localization in vivo.

ATOMS concept

MRI measures signals from ensembles of nuclear spins, each of which can be thought of as an atom-sized transmitter resonating at a magnetic field dependent frequency (Fig. 1a). A magnetic field gradient is applied such that spins in one location resonate at a predictably different frequency from spins at another location. Applying gradients while receiving signal from the full ensemble of nuclei allows the use of frequency shifts to assign signals to specific locations in space. Conversely, one can excite spins selectively by applying field gradients during frequency-specific transmission.

We reasoned that by creating silicon ATOMS circuits that mimic the behaviour of nuclear spins, we would be able to localize devices containing such circuits in space using magnetic field gradients (Fig. 1b). This would allow the devices to transmit information or receive commands via RF signals in a spatially specific

[1]Division of Engineering and Applied Sciences, California Institute of Technology, Pasadena, CA 91125, USA. [2]Division of Chemistry and Chemical Engineering, California Institute of Technology, Pasadena, CA 91125, USA. *e-mail: mikhail@caltech.edu; azita@caltech.edu

manner (Fig. 1c). Similarly to nuclear spins in MRI, this approach could allow multiple identical devices at different locations to be addressed in parallel, wherein ATOMS devices at different locations transmit and receive signals at distinct frequency shifts. Importantly, unlike MRI, a strong static polarizing magnetic field is not required, as ATOMS oscillations can be powered by internal or external energy sources. Also, unlike other RF localization methods, the spatial resolution of this approach would not be limited by RF wavelengths or tissue parameters.

In this work, we provide a proof of concept for the basic capabilities of ATOMS by designing, developing and testing an integrated circuit capable of encoding its position inside a magnetic field gradient in its oscillation frequency, and demonstrating 2D localization using frequency encoding. As discussed below, this core capability serves as the basis for engineering future ATOMS devices that can be addressed spatially in three dimensions using techniques analogous to MRI pulse sequences—frequency encoding, phase encoding and selective excitation—to be combined with separately developed local sensing and actuation functionality.

The basic operation of our proof-of-concept device consists of three phases: the magnetic, excitation and transmission phases (Fig. 1d). During the magnetic phase, ATOMS devices sense, process and store the applied magnetic field at each of their locations. The excitation phase starts when the RF pulse is applied. The frequency of the RF pulse f_0 is acquired, and the devices start oscillating at the same frequency. The transmission phase follows, during which each device emits a signal with a shifted frequency proportional to the measured magnetic field.

Results

ATOMS chip architecture. The system architecture of our ATOMS chip consists of a magnetic sensor, a two-stage chopper amplifier, an analog-to-digital converter (ADC), a phase-locked loop (PLL), a power amplifier (PA), an on-chip coil, and a control logic with digital signal processing (DSP) (Fig. 2a). A base frequency of 500 MHz (f_0) was chosen based on compatibility with available equipment.

The magnetic sensor is an on-chip split-drain magnetic field-sensitive field-effect transistor (MagFET) that measures the applied magnetic field orthogonal to the chip (B_Z). This Hall-effect device generates a differential current ΔI proportional to B_Z and the bias current I_{MS}[35]. The MagFET's output is amplified by a trans-impedance amplifier (TIA) and a low-noise amplifier (LNA). To minimize noise at low frequencies, a chopper amplifier is formed by adding chopper modulators in the TIA and the LNA. The output of the
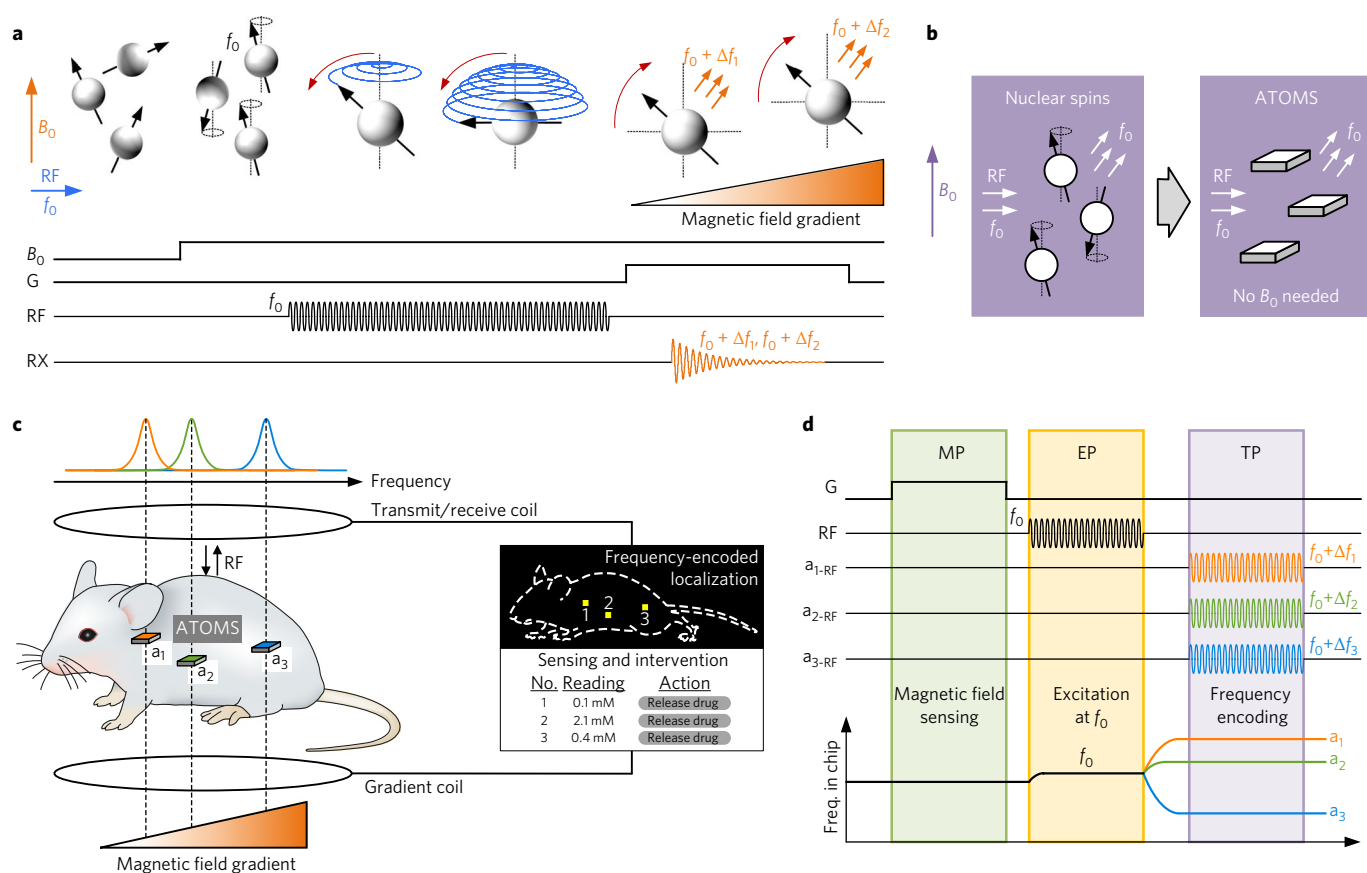
Fig. 1 | ATOMS concept. a, The operating principle of MRI. When a polarizing magnetic field (B_0) is applied, randomly oriented nuclear spins align to B_0 and start precessing at a known frequency f_0 (Larmor frequency). Then, after excitation by an RF signal at f_0, the nuclear spins radiate back a signal at a frequency that is shifted relative to f_0 proportional to an applied magnetic field gradient. Thus, their location can be determined by mapping the received signals in space. **b**, Addressable transmitters operated as magnetic spins (ATOMS) mimic the behaviour of nuclear spins in MRI. It is important to note that B_0 (the magnetic field generated by the superconductive MRI magnet) is not required. **c**, ATOMS are microscale devices capable of power harvesting and communication at magnetic field-dependent frequencies. When multiple ATOMS are in an animal or patient, their locations are discerned by applying a magnetic field gradient. Three separate ATOMS chips are labelled a1, a2 and a3. **d**, ATOMS sense and store the applied magnetic field at each of their locations before excitation. When the RF signal is applied, they start oscillating at the same frequency f_0. After the RF excitation is turned off, they emit a signal with a shifted frequency proportional to the measured magnetic field. MP, magnetic phase; EP, excitation phase; TP, transmission phase.
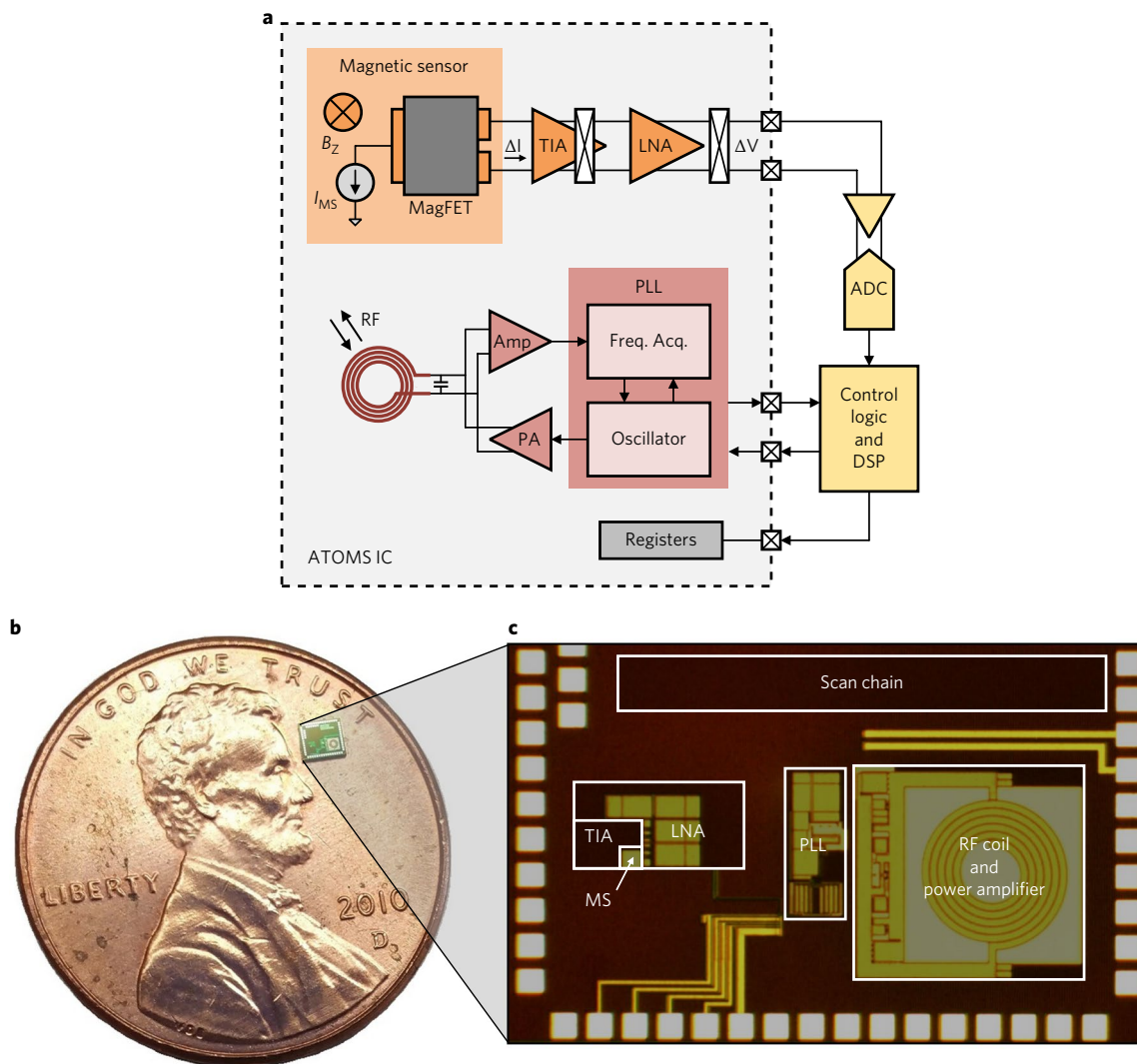
Fig. 2 | ATOMS chip architecture. a, A schematic of an ATOMS device. An on-chip magnetic field-sensitive field-effect transistor (MagFET) measures the applied magnetic field orthogonal to the chip. Its output is amplified and digitized for processing. An on-chip coil acquires the RF excitation signal and emits the response of the chip, which is a signal with a shifted frequency proportional to the measured magnetic field. A phase-locked loop (PLL) is used to lock the internal oscillator to the RF signal. TIA, trans-impedance amplifier; LNA, low-noise amplifier; ADC, analog-to-digital converter; DSP, digital signal processing; PA, power amplifier. **b,c**, ATOMS microchip compared with a US penny (**b**) and die micrograph (**c**). The chip is 1.8 × 1.2 mm. MS, magnetic sensor.

amplifier is then digitized for processing (for example, averaging) and storage. The on-chip coil acquires the excitation RF signal and emits the response of the chip. The PLL uses a ring oscillator instead of an LC oscillator to reduce area and power consumption at the expense of higher phase noise. However, the phase noise constraints can be relaxed by adjusting the bandwidth of the external receiver. An oscillation detector is included to sense the presence of the RF pulse and to enable control of the PLL loop. During the excitation phase, the chip closes this loop for frequency acquisition and synchronization, where the PLL locks the internal oscillator to the RF pulse. During the transmission phase, the chip opens the PLL loop, shifts the frequency of the internal oscillator proportional to the measured magnetic field, and feeds the oscillator's output to the PA for transmission. To generate frequency shifts, a current digital-to-analog converter with a 6-bit resolution is used. The control logic manages the whole operation of the chip and processes the measured magnetic field.

In this work, we focus on integrating the critical components of the system in a single chip: the magnetic sensor, amplifiers, PLL, PA

and the on-chip coil for frequency locking and radiation. The ADC and control logic have more relaxed requirements due to the low processing speed (up to a few kHz), and can be integrated into the system in future versions with minimal impact on size and power requirements. The chip was fabricated in a standard 180 nm CMOS process and occupies an area of 1.8 × 1.2 mm (Fig. 2b,c).

The on-chip MagFET has a size of 20 × 28 µm, a measured sensitivity of 3.29% T^{-1} (defined as $\Delta I/I_{MS}B_Z$), and a measured total input referred noise of 625.48 µT between 2 Hz and 100 kHz. The TIA and LNA have a gain of 317.38 kΩ and 25 dB, respectively. The overall bandwidth of the amplifier is 1 kHz, and the chopper frequency is set to 763 Hz. These results translate to a sensitivity of 5.48 V T^{-1} at the output of the LNA. The on-chip coil has a size of 420 × 420 µm and a quality factor of 4.6 at 500 MHz. The PLL has an integrated root mean square jitter (10 kHz–10 MHz) of 60 ps when it is locked and 308 ps when it is unlocked. The minimum frequency shift is set to 1.4 MHz for a total range of 88.5 MHz centered at f_0. The power consumption of the chip is dominated by the magnetic sensor, the internal oscillator and the radiation elements, and it is measured to
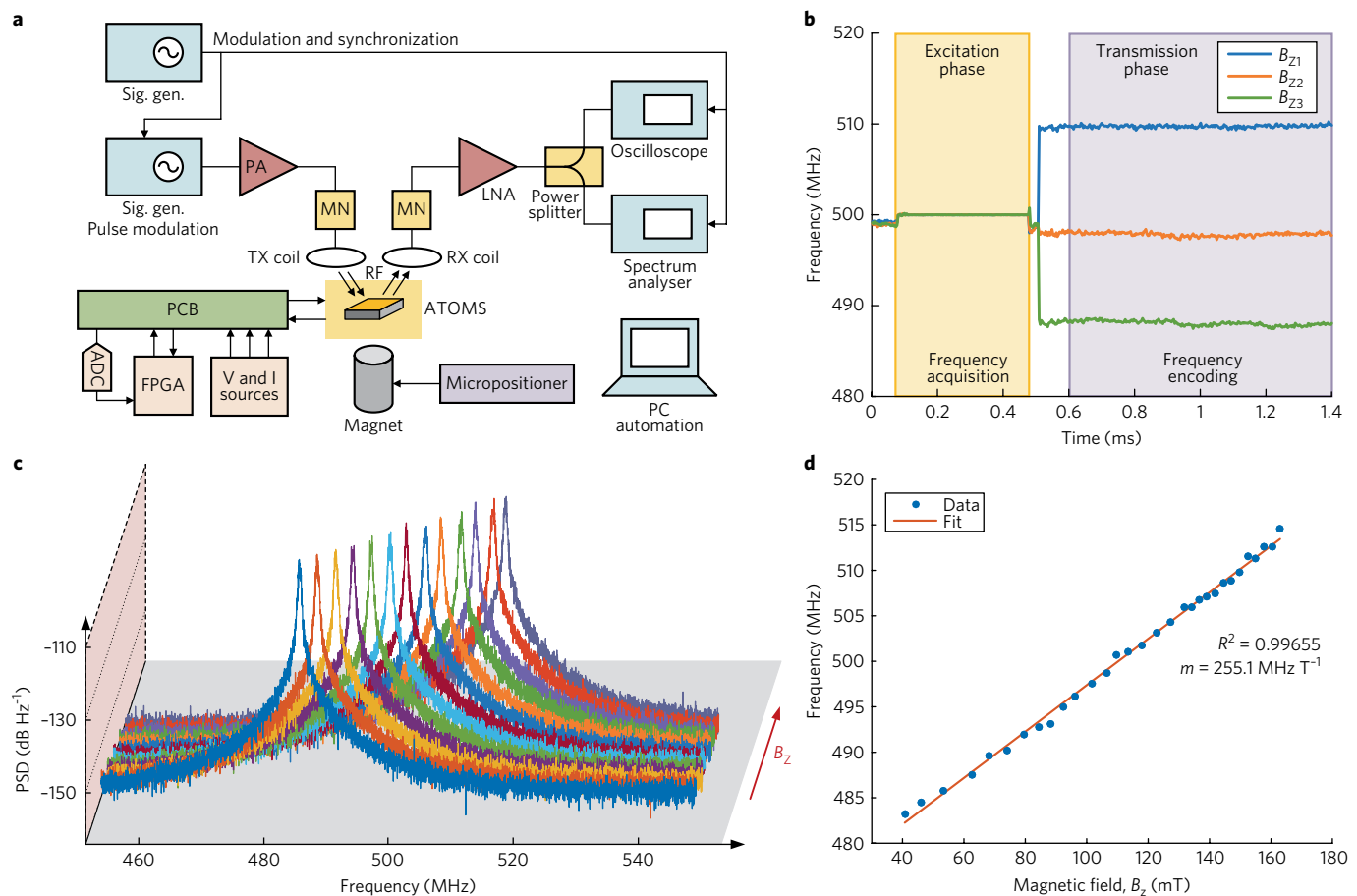
Fig. 3 | Electrical characterization. a, An illustration of the test setup for ATOMS characterization. The ATOMS chip was exposed to 31 different values of the magnetic field. A permanent magnet was used to generate the magnetic field gradient. The excitation RF signal with a pulse width of 400 µs was produced using a signal generator. The response of the chip was captured by a receive coil, amplified by an LNA, and analysed using a spectrum analyser and a real-time oscilloscope. The receiver reading window was set to 800 µs. A second signal generator was used for pulse modulation and synchronization between transmitter and receiver channels. Sig. gen., signal generator; MN, matching network; FPGA, field-programmable gate array; PCB, printed-circuit board; V, voltage; I, current; PC, personal computer. **b**, Frequency response during excitation phase and transmission phase, showing frequency acquisition and frequency encoding for three magnetic field magnitudes. **c**, Spectral profile of the ATOMS chip at 13 magnetic field strengths, showing the power spectral density (PSD) as a function of frequency. The arrow indicates an increase in the magnetic field B_Z. **d**, Oscillation frequency of the chip as a function of the magnetic field and its linear regression.

be 339 µW on average. While power is provided externally in this design, such low power consumption allows wireless power delivery in future versions. An external ADC with 12-bit resolution and sample rate of 763 Hz is used for all our measurements. The control logic and DSP are implemented in an external field-programmable gate array (FPGA). The controller runs at 1 MHz to transmit 150 bits via a serial interface, and the DSP runs at 763 Hz.

Electrical characterization of the ATOMS chip. We characterized the performance of the ATOMS chip using the test setup shown in Fig. 3a. The chip was placed in a printed circuit board (PCB) to connect to the ADC, FPGA and power supplies. We used the wired output of the chip to only measure and evaluate the response of the system during the excitation phase in initial electrical characterization. All other measurements were taken from the wireless signal picked up by the external receiver coil. We used a permanent magnet to generate the magnetic field gradient, which was mapped using a gaussmeter.

The ATOMS chip first measured the local magnetic field and used a moving-average filter of 128 samples at 763 Hz (implemented in the FPGA) to reduce noise. The internal oscillator, during this

phase, oscillated at its natural frequency. When the excitation RF pulse (400 µs pulse width) was applied, the chip wirelessly detected its presence, locked the internal oscillator to this signal, and measured its frequency. When the RF pulse was removed, the chip sensed this transition and shifted its oscillation frequency for transmission (Fig. 3b). Note that the latency in communication between the chip and the external control logic (FPGA) caused a delay of ~35 µs in frequency encoding due to the use of a serial interface for data transfer; during this time the PLL was opened and the oscillation frequency briefly returned to its initial value. For this experiment, the output of the chip was measured for 800 µs at 31 different values of the magnetic field using a real-time oscilloscope with a sampling rate of 10 GHz.

The spectral profile of the chip at thirteen magnetic field strengths is shown in Fig. 3c. As expected, the oscillation frequency of the chip changed proportional to the field strength. It showed a full width at half maximum (FWHM) or 3 dB bandwidth of 600 kHz. A linear relationship between oscillation frequency and magnetic field was revealed in the range of 480–520 MHz and 40–170 mT (Fig. 3d). For each field strength, the oscillation frequency was estimated by calculating the centre frequency of the peak of the power spectral
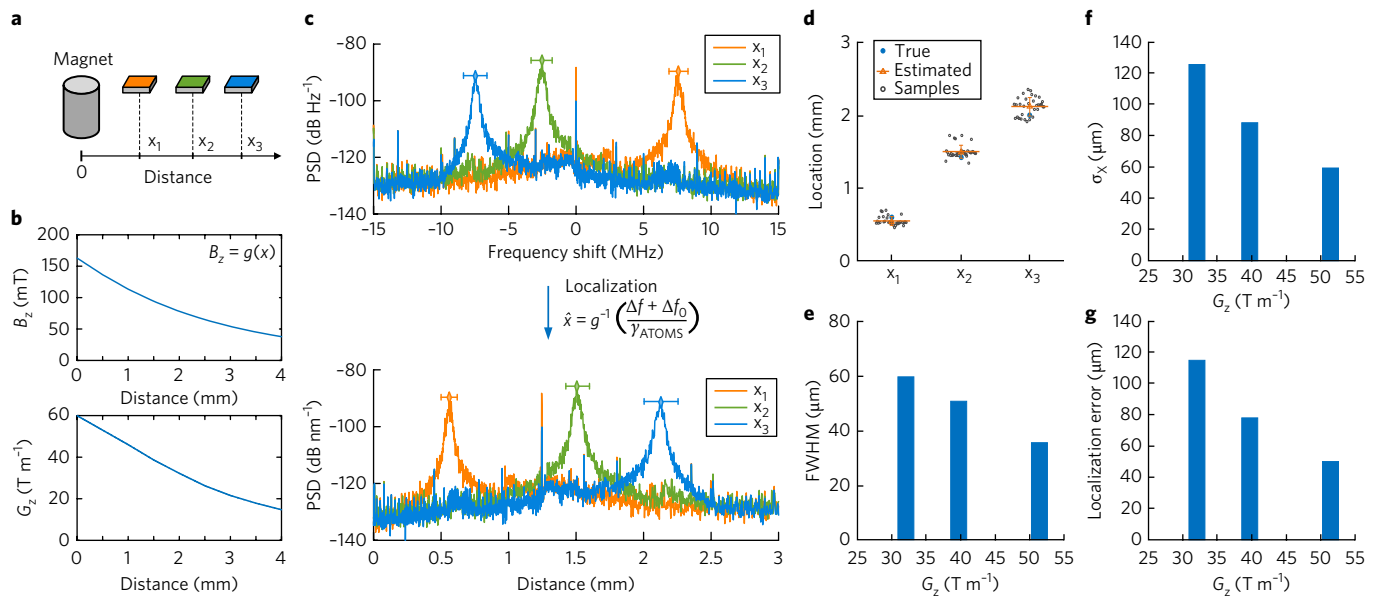
Fig. 4 | 1D localization of the ATOMS chip. a, An illustration of the 1D localization experiment with three different positions for the ATOMS chip. **b**, Magnetic field and magnetic field gradient produced by the magnet. Note the definition of B_z as $g(x)$. **c**, Frequency shift-location estimation. The figure shows the PSD of the received signal as a function of frequency shifts (top) and distance (bottom). The location was estimated by mapping the pre-measured magnetic field back in space according to Δf, γ_{ATOMS} and the inverse function g^{-1}. Error bars indicate the standard deviation of the peak of the PSDs. Interference at the centre frequency (500 MHz) due to harmonics of electronics' clock signal was filtered out during processing. **d**, Localization results showing the estimated and true positions for all three cases. Circles represent all data points. Error bars represent ±s.d. **e**, FWHM of the spatial PSD as a function of the field gradient G_z. **f,g**, Standard deviation σ_x of the location measurements shown in **d** (**f**), and the localization error of the experiment (**g**). The location was estimated by taking the average of the centre value of the peak of the spatial PSD (**c**, bottom, 32 measurements). FWHM, full-width at half-maximum or 3 dB bandwidth. $N = 32$ for **c,d**.

density (PSD); then a linear fit was calculated. We defined a parameter to represent the relationship between the oscillation frequency of the device and the magnetic field, calling it its gyromagnetic ratio, γ_{ATOMS}, by analogy to nuclear spins. The ATOMS chip has a measured γ_{ATOMS} of 255.1 MHz T^{-1}.

1D localization. To evaluate the spatial localization performance of ATOMS, we first performed a 1D localization experiment using the test setup described above, with the chip at 3 different positions along the same axis (Fig. 4a). The magnetic field profile generated by the permanent magnet, $B_z = g(x)$, is shown in Fig. 4b. The chip's output signal, whose frequency shifted according to the field at its location and γ_{ATOMS}, was measured wirelessly. As expected, the chip generated different frequency shifts Δf for each position (Fig. 4c). We could then obtain the location of the device according to:

$$\hat{x} = g^{-1}\left(\frac{\Delta f + \Delta f_0}{\gamma_{ATOMS}}\right) \qquad (1)$$

where g^{-1} is the inverse function of B_z and Δf_0 is the frequency shift offset (Supplementary Fig. 1). The resulting localization is shown in Fig. 4c (bottom). Notably, the width of the spectral response at each position increased with distance from the permanent magnet due to the field gradient decreasing as a function of this distance. The position of the chip was estimated as the centre value of the peak of the PSD in space. The true and estimated positions for all three locations, and the FWHM as a function of the magnetic field gradient are shown in Fig. 4d,e. The standard deviation of the estimated location σ_x across 32 independent measurements and the error of the estimate relative to the true location at each point are shown in Fig. 4f,g. Both quantities increased in inverse proportion

to the magnetic field gradient at each location, from 50.44 µm and 59.17 µm when the gradient is 51.46 T m^{-1} to 115.4 µm and 125.7 µm when it is 32.14 T m^{-1}, respectively.

2D localization. Next, we performed a 2D localization experiment using the test setup shown in Fig. 5a. We used two permanent magnets (M_1 and M_2) to apply magnetic field gradients in two different directions (Fig. 5b,c). Adding and removing one magnet at a time allowed us to apply a sequence of two field gradients, analogous to the design of pulse sequences in MRI. The frequency response of the chip in each gradient defined a curve of possible positions corresponding to a specific magnetic field magnitude (B_{Z_1} and B_{Z_2} in Fig. 5a). We defined the functions $P_{M_1}(x,y)$ and $P_{M_2}(x,y)$ as the mapping of the PSD of the chip's response into the 2D magnetic field space of M_1 and M_2, respectively. We then obtained the 2D position from the centre of the peak of $P_{M_{12}}(x,y) = \left(P_{M_1}/P_{M_1,max}\right)\left(P_{M_2}/P_{M_2,max}\right)$, representing the point of intersection.

We used this system to track the location of an ATOMS chip while translating it in space to write the letters C, I and T. As expected, the three letters can be clearly identified (Fig. 5d). The estimated and true positions of the ATOMS chip at each measurement point are shown in Fig. 5e. A localization error of less than 250 µm was measured for all cases (Fig. 5f). Similar to the previous experiment, the error depended on the magnitude of the magnetic field gradient, with lower errors where the gradient is highest.

In vivo localization. To establish the feasibility of ATOMS technology within the context of in vivo biological tissue, we localized our ATOMS device following subcutaneous implantation in an anesthetized mouse (Fig. 6a). In preparation for this experiment, the chip was placed in the shaft of a small PCB and encapsulated using a silicon elastomer. We moved the chip to four different locations on
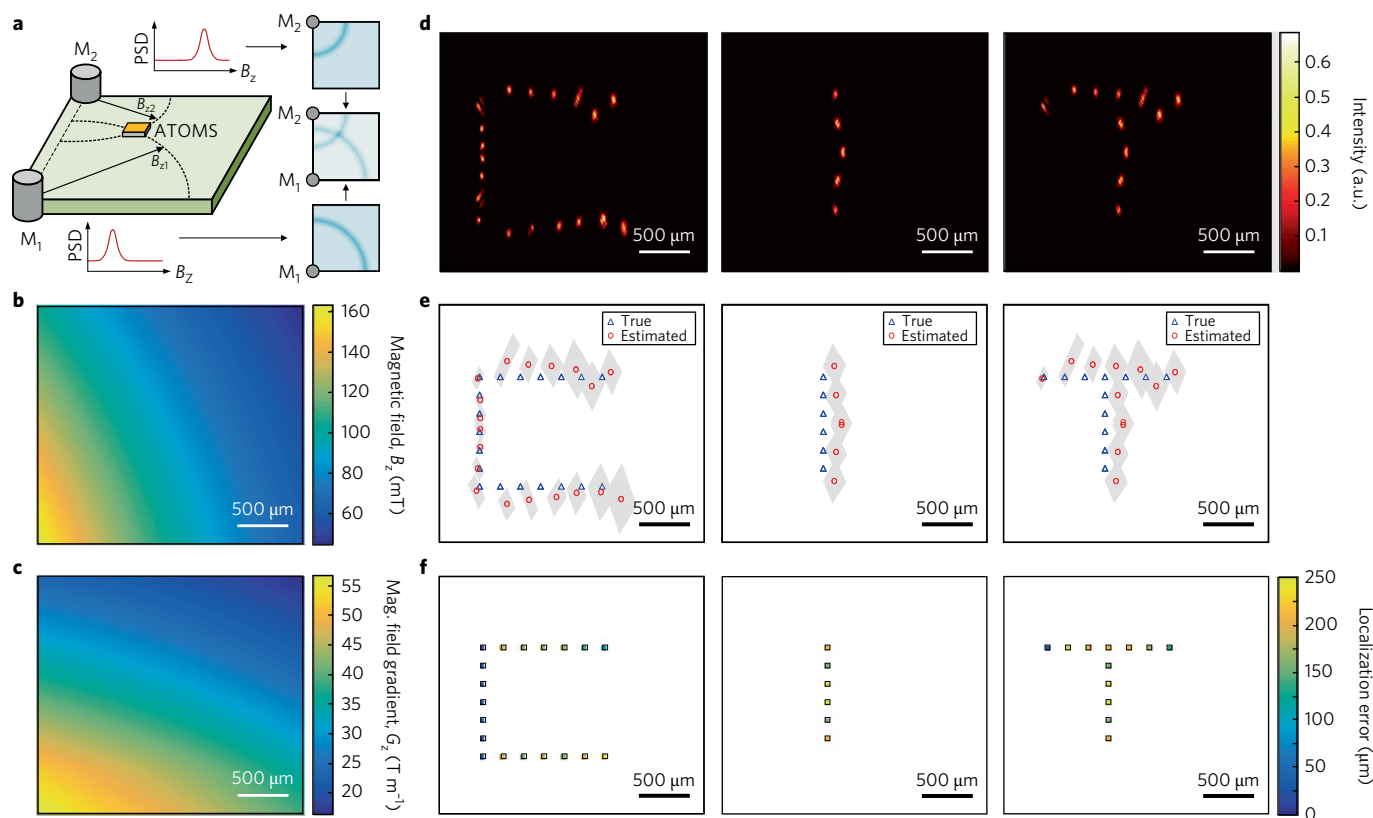
Fig. 5 | 2D localization of the ATOMS chip. a, Illustration of the 2D localization experiment, in which two magnets were used to generate two magnetic field gradients in different directions. The ATOMS chip was moved relative to the position of both magnets. At each location, the distance to each magnet was estimated using a single magnet at a time. The 2D location was then determined by combining both estimated distances. **b,c,** 2D mapping of the magnetic field (**b**) and magnetic field gradient (**c**) generated by the magnets. The magnets were placed at locations (0,0) mm for M_1 and (0,2.6) mm for M_2. Only M_1 is shown as both magnets are of the same kind. Colour bars indicate the magnetic field in mT and the magnetic field gradient in T m^{-1}. **d,** Localization results of three different experiments where the ATOMS chip was placed at positions to form the letters C, I, T. Colour bar indicates intensity. **e,** The estimated and true positions of each experiment. The shaded region indicates the standard deviation. **f,** Localization errors of each experiment. Each square in the figure shows the error of its corresponding position in space. Colour bar indicates the error in μm. $N = 32$ for **e**.

a single axis using a micropositioner. A stronger magnet was used to increase the effective field of view (FOV) to more than 12 mm by generating the magnetic field profile shown in Fig. 6b. Due to this new profile, the chip was tuned to accommodate the new magnetic field range by calibrating the magnetic sensor offset and reducing the overall gain of the system. In this case, γ_{ATOMS} was measured to be 170.7 MHz T^{-1}. The PSD of the received signals exhibited four different peaks corresponding to the target locations (Fig. 6c). A localization error of less than 500 μm was measured for all cases (Fig. 6d,e), and this error exhibited less positional dependence than previous experiments, in agreement with the more linear magnetic field. This experiment demonstrates that ATOMS-enabled devices can be localized in living biological tissues.

Discussion

In this study, we introduce the concept of ATOMS—microscale devices that mimic the behaviour of nuclear spins to enable their spatial localization using the principles of magnetic resonance—and demonstrate the core element of this concept in vitro and in vivo. The ATOMS technology provides an elegant solution to the problem of locating and interfacing with microscale in vivo biosensors by decoupling the dependence of RF methods from body composition and time-sensitive parameters (for example, time of arrival or strength of received signal). As a result, it combines the benefits of frequency encoding using magnetic field gradients and highly

sensitive RF receivers. Because ATOMS technology does not require a superconductive magnet, it offers a more affordable and simpler alternative compared to actual MRI methods that image nuclear spin precession.

The methods developed in this work can be extended to 3D localization of microscale devices using techniques similar to MRI pulse sequences (Supplementary Fig. 2). For a single ATOMS device inside a patient, 3D localization can be achieved by using a sequence of three magnetic field gradients in different directions (G_X, G_Y and G_Z) and performing frequency encoding in each dimension. For multiple ATOMS devices, 3D localization can be accomplished by using selective excitation, phase encoding and frequency encoding. For instance, selective excitation can be performed by applying G_Z such that devices outside the slice of interest become inactivated for transmission by experiencing field magnitudes above a certain threshold. Phase encoding can be achieved by producing a phase shift (using a digitally controlled phase shifter) proportional to the magnetic field generated by G_Y. Finally, frequency encoding can be performed by applying G_X as described in the previous sections.

In the case of an angular misalignment of $\theta°$ between B_Z and the ATOMS device, a localization error can occur because the magnetic sensor measures the magnetic field orthogonal to its surface (that is, $B_Z\cos\theta$). To overcome this limitation, we can add an extra step in the pulse sequence where a uniform magnetic field B_C is applied to provide
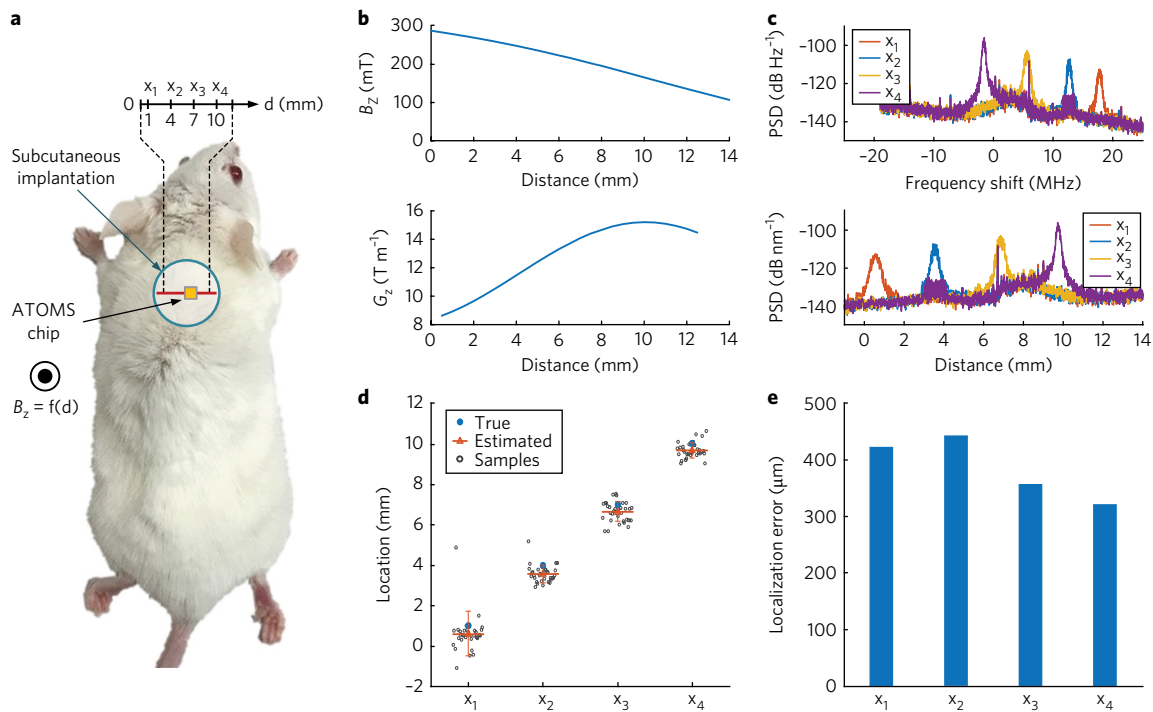
Fig. 6 | In vivo localization. a, An illustration of the in vivo localization experiment. The ATOMS chip was implanted subcutaneously in the shoulder area of an anesthetized mouse, placed at four different locations. A permanent magnet placed above the mouse generated the magnetic field profile, and a transmit/receive coil was used for RF excitation and signal reception. **b,** Magnetic field and magnetic field gradient produced by the magnet. **c,** Frequency shift-location mapping. The figure shows the PSD of the received signal as a function of frequency shift (top) and distance (bottom). **d,** Estimated and true positions of all 4 cases. Circles represent all data points. **e,** Localization error of the experiment. $N = 32$ for **d.** Error bars represent $\pm$s.d.

a correction factor for measuring B_{G_Z}, the magnetic field generated by G_Z at the location of the chip (Supplementary Fig. 3). In this scheme, we first apply the reference field B_C, and the device responds with a frequency shift Δf_{MC}, generated by the measured magnetic field $B_{MC} = B_C \cos\Theta$. We then apply G_Z, and the device responds with Δf_{MZ}, generated by $B_{MZ} = B_{GZ} \cos\Theta$. Using both measurements, B_{G_Z} can be obtained from $B_C \Delta f_{MZ}/\Delta f_{MC}$ (see Supplementary Material for detailed derivation). This approach allows the correct estimation of the chip's location and orientation as long as the local magnetic fields perpendicular to the chip, B_{MC} and B_{MZ}, are above the noise floor of the magnetic sensor. For a single device, B_C and G_Z can be applied in two successive acquisitions. For simultaneous localization of multiple devices, both fields are applied consecutively in a single acquisition, where each device calculates the ratio of B_{MZ} and B_{MC} internally and responds with a frequency shift proportional to this ratio. Another approach is to use a 3D magnetic sensor in the chip. In this case, B_{G_Z} can be calculated by measuring all three components of the magnetic field and performing frequency encoding with the total field. Both methods can also be applied to phase encoding.

The noise of the magnetic sensor and the phase noise of the oscillator are the main factors that affect the minimum detectable frequency shift Δf_{min} and, therefore, the resolution of the system. It can be shown that, for frequency encoding, the theoretical spatial resolution is given by

$$\Delta x = \frac{\Delta f_{min}}{\gamma_{ATOMS} G_Z} \qquad (2)$$

where $\Delta f_{min} = 2\sigma_f$, and σ_f is the standard deviation of the oscillation frequency (see Supplementary Material for detailed derivation).

The resolution of our current in vivo system would be limited to 360 μm ($\gamma_{ATOMS} = 170.7$ MHz T^{-1}, $G_Z = 9$ T m^{-1}). It is important to note that, in our current design, the magnetic sensor noise and oscillator phase noise are limited by the small power consumption befitting a wirelessly powered implantable device. Applications such as capsule endoscopy or minimally invasive surgery[1,3,5], in which power can be supplied externally or via battery, present higher power budgets that would boost the performance of the sensor and oscillator, and therefore the resolution of the system.

The strength of the magnetic field gradient also impacts the localization resolution. Our experiments show an in vivo accuracy of ~500 μm when the field gradient is ~10 T m^{-1}. Therefore, in our current implementation, a magnetic field gradient of ~5 T m^{-1} is required for 1 mm resolution. Field gradients of this magnitude are already in use in magnetic particle imaging instruments, with values as high as 7 T m^{-1} (ref. [36]). This resolution is larger than the MagFET sensor on our chip, meaning that localization is currently limited by noise rather than device dimensions.

The size of a fully wireless ATOMS device depends on the power delivery method and communication requirements. For instance, on-chip integration of RF power delivery components limits device size to the area of the power antenna. Current approaches use frequencies in the range of 0.9–2 GHz, which maximize power transfer to microscale devices in tissue[37,38], and use antennas with <2 mm^2 areas[38,39]. With a thickness of 100 μm, the size of a device incorporating such an antenna would be ~0.2 mm^3. Alternative power delivery methods, such as a battery or piezoelectric powering, could have a smaller footprint on the device, in which case device size would be limited by the on-chip radiating antenna used for communications. In our current device, this antenna has an area of ~0.2 mm^2, which could be reduced at higher frequencies (single GHz range). Using the power requirements of our current device and available battery

technology, with capacities greater than 65 μWh mm^{-3} (refs [40–42]) an ATOMS device incorporating a battery smaller than 0.01 mm^3 could make more than 1,000 location measurements during its transit through the body (each measurement lasting 5 ms), such that total device size could be close to 0.03 mm^3. Incorporation of control logic and ADC onto a fully wireless chip is not expected to significantly impact device dimensions or power requirements, since these circuit elements operate at kHz frequencies and can be designed to consume less than 1 μW while occupying areas smaller than 0.017 mm^2 and 0.01 mm^2, respectively[43,44].

The in vivo experiments presented in this study provide a rudimentary proof of concept for magnetic gradient spatial encoding and RF communication in living tissue. Future experiments are needed to establish the range of possible ATOMS applications in light of parameters such as RF absorption and tissue movement. RF absorption in deep tissues will determine the size and power requirements of ATOMS antennae, with the estimates discussed above valid to depths of a few centimetres[37,38]. Device motion inside the body will affect the spatial precision of localization. However, the timescales for performing a MagFET measurement, locking into a base frequency, and radiating a position-dependent signal, on the order of single ms, are well below the relevant timescales of breathing, heartbeat and gastrointestinal peristalsis. The fastest of these, cardiac wall motion, has a speed of ~50 mm s^{-1} in humans[45], which would allow for a 20 ms ATOMS interaction to preserve sub-millimetre spatial precision. Although rotational motion could also play a role in ATOMS devices using a reference field measurement to account for MagFET alignment, rotation is expected to be severely restricted in most tissues for micrometre-to-millimetre scale devices.

With precise localization in vivo, ATOMS-enabled devices can act as real-time sensors and actuators for diagnosis and therapy. For sensors, information about the measured quantity can be encoded in the device's transmitted output via amplitude or time modulation. For actuators, slice selection in three dimensions can activate a therapeutic event for ATOMS-enabled devices located only at a specific spot in the body.

Outlook

In summary, our results establish the concept of microscale silicon devices mimicking the physical behaviour of nuclear spins to enable their localization inside the body, and provide a proof of concept by localizing a device smaller than 0.7 mm^3 in vivo with sub-millimetre precision. The ATOMS technology combines the benefits of RF communication with the simple spatial encoding offered by magnetic-field gradients. In addition, it enables external control and adaptation of the spatial resolution by programming of γ_{ATOMS} and G_Z. The integration of ATOMS with microscale biological sensing and actuation technologies will enhance the development of a wide range of biomedical applications, from distributed localized monitoring of biologically relevant biomarkers to targeted release of therapeutic agents and tissue imaging for disease diagnosis.

Methods

Test setup for bench experiments. The ATOMS chip was placed in a small daughter PCB and connected using wirebonds. This PCB was connected to a mother PCB which interfaces with the ADC, FPGA, and voltage and current sources. The PCBs were fabricated on a standard 4-layer 0.062" FR4 substrate. The outputs of the chip's LNA were buffered using an AD8512 dual amplifier from Analog Devices in a voltage-follower configuration. The buffered outputs of the chip were digitized by an AD7450 12-bit ADC from Analog Devices. The FPGA was a Cyclone IV EP4CE115F29C7 from Altera, and was integrated in a DE2-115 development board from Terasic. The FPGA interfaced directly with the ADC, processed the digitized data and controlled the operation of the chip. The FPGA code was written in Verilog HDL. A MSO7104B mixed-signal oscilloscope from Keysight was used to visualize the output of the chip and other control signals.

The RF pulse was applied via a 4-turn coil which was connected to a matching network. The coil had a diameter of 5 mm and was manually wounded using

copper wire with a diameter of 320 μm. The coil was aligned with the chip and placed at ~3 mm distance from it. The RF signal was generated by a MG3694B signal generator from Anritsu and was amplified by a ZHL-20W-13SW + power amplifier from MiniCircuits. Semirigid coaxial cables were used to connect the coil and matching network to the output of the power amplifier. The RX channel used a second coil which is similar to the transmit coil. A similar matching network was also used. The signal from the chip was picked up by the coil and amplified by a chain of 3 ZX60-P33ULN + low-noise amplifier from MiniCircuits. The output of the amplifier is sent to a DSA90804A real-time oscilloscope and an E4440A spectrum analyser, both from Keysight. Pulse modulation of the RF signal and synchronization between TX and RX channels were performed using a Keysight 33522B waveform generator. The whole test setup was automated and controlled by a custom script written in MATLAB. The magnetic field was generated using an NdFeB grade N40 magnet from MAGCRAFT, with a size of 0.5" diameter × 1" length. The distance between the chip and the magnet was controlled by moving the magnet using a micropositioner.

Test setup for in vivo experiments. For the in vivo experiment, the interface with the chip was modified as follows. A small PCB with a shaft on a standard 4-layer 0.062" FR4 substrate was designed to hold the chip for insertion. The shaft had a length of 32 mm and a width of 3.55 mm before encapsulation. The chip was placed in the tip of the PCB's shaft and both were encapsulated using a silicon elastomer. The total width of the shaft after encapsulation was 4 mm. The PCB with the chip was inserted into the mouse and moved to target locations using a micropositioner. A shielded cable was used to connect this small PCB to the mother board and the rest of the test setup. The magnetic field was generated using an NdFeB grade N52 magnet from K&J Magnetics, with a size of 2" diameter × 2" length. The magnet was placed above the mouse. A transmit/receive coil was used to send the RF pulse and to pick up the response of the chip. Custom 3D-printed structures were designed to hold and position the small PCB, magnet and animal in place.

Chip silicon encapsulation. First, a layer of Sylgard-184 was applied on top of the chip to cover and protect the wirebonds, and it was cured at 75 °C for 60 min. Silastic MDX4-4210 was then used for encapsulation. Dip-coating was performed on the PCB's shaft with the chip, and it was cured at 75 °C for 60 min.

Animal procedures. A small incision of 1.5 cm was made in the skin of the shoulder area of a female BALB/c wild-type mouse (>30 weeks old) to insert the microchip. The mouse was anaesthetized during the entire experiment with an IP injection of ketamine/xylazine (100 and 10 mg kg^{-1} of BW, respectively). The incision area was shaved and cleaned before insertion of the microchip. An RF signal and a magnetic field was applied using a small antenna and a permanent magnet. The chip measured these signals and then radiated an RF signal back. This signal was picked up by the antenna to be analysed. The signal was measured for 5 min per location. A total of 4 locations were measured. One mouse was used in these experiments, since this was adequate to demonstrate device performance. This animal procedure was approved by the Institutional Animal Care and Use Committee of the California Institute of Technology.

Data and statistical analysis. The detection algorithm, fits and measurement figures were written and generated in MATLAB running on a standard workstation. Where replicate measurements were performed, the sample size was selected based on preliminary experiments to provide sufficient data for calculation of mean and standard deviation.

Code availability. Code used in this study is available from the authors upon request.

Data availability. The authors declare that all data supporting the findings of this study are available within the paper and its Supplementary Information.

References

1. Sitti, M. et al. Biomedical applications of untethered mobile milli/microrobots. *Proc. IEEE* **103**, 205–224 (2015).
2. Bergeles, C. & Yang, G. Z. From passive tool holders to microsurgeons: safer, smaller, smarter surgical robots. *IEEE Trans. Biomed. Eng.* **61**, 1565–1576 (2014).
3. Ciuti, G., Menciassi, A. & Dario, P. Capsule endoscopy: from current achievements to open challenges. *IEEE Rev. Biomed. Eng.* **4**, 59–72 (2011).
4. Yim, S., Gultepe, E., Gracias, D. H. & Sitti, M. Biopsy using a magnetic capsule endoscope carrying, releasing, and retrieving untethered microgrippers. *IEEE Trans. Biomed. Eng.* **61**, 513–521 (2014).
5. Ciuti, G. et al. Frontiers of robotic endoscopic capsules: a review. *J. Micro-Bio Robot.* **11**, 1–18 (2016).

6. Alivisatos, A. P. et al. Nanotools for neuroscience and brain activity mapping. *ACS Nano* **7**, 1850–1866 (2013).
7. Seo, D. et al. Wireless recording in the peripheral nervous system with ultrasonic neural dust neuron neuroresource wireless recording in the peripheral nervous system with ultrasonic neural dust. *Neuron* **91**, 529–539 (2016).
8. Williams, B. J., Anand, S. V., Rajagopalan, J. & Saif, M. T. A self-propelled biohybrid swimmer at low Reynolds number. *Nat. Commun.* **5**, 3081 (2014).
9. Nelson, B. J., Kaliakatsos, I. K. & Abbott, J. J. Microrobots for minimally invasive medicine. *Annu. Rev. Biomed. Eng.* **12**, 55–85 (2010).
10. Liu, L., Towfighian, S. & Hila, A. A review of locomotion systems for capsule endoscopy. *IEEE Rev. Biomed. Eng.* **8**, 138–151 (2015).
11. Than, T. D., Alici, G., Zhou, H. & Li, W. A review of localization systems for robotic endoscopic capsules. *IEEE Trans. Biomed. Eng.* **59**, 2387–2399 (2012).
12. Pourhomayoun, M., Jin, Z. & Fowler, M. L. Accurate localization of in-body medical implants based on spatial sparsity. *IEEE Trans. Biomed. Eng.* **61**, 590–597 (2014).
13. Ye, Y., Pahlavan, K., Bao, G., Swar, P. & Ghaboosi, K. Comparative performance evaluation of RF localization for wireless capsule endoscopy applications. *Int. J. Wirel. Inf. Networks* **21**, 208–222 (2014).
14. Chandra, R., Johansson, A. J., Gustafsson, M. & Tufvesson, F. A microwave imaging-based technique to localize an in-body RF source for biomedical applications. *IEEE Trans. Biomed. Eng.* **62**, 1231–1241 (2015).
15. Bao, G., Pahlavan, K. & Mi, L. Hybrid localization of microrobotic endoscopic capsule inside small intestine by data fusion of vision and RF sensors. *IEEE Sens. J.* **15**, 2669–2678 (2015).
16. Hu, C. et al. A cubic 3-axis magnetic sensor array for wirelessly tracking magnet position and orientation. *Sensors J. IEEE* **10**, 903–913 (2010).
17. Schlageter, V., Besse, P. A., Popovic, R. S. & Kucera, P. Tracking system with five degrees of freedom using a 2D-array of Hall sensors and a permanent magnet. *Sensors Actuat. A Phys.* **92**, 37–42 (2001).
18. Schlageter, V., Drljaca, P., Popovic, R. S. & Kucera, P. A magnetic tracking system based on highly sensitive integrated Hall sensors. *JSME Int. J. Ser. C* **45**, 967–973 (2002).
19. Wu, X. et al. Wearable magnetic locating and tracking system for MEMS medical capsule. *Sensors Actuat. A Phys.* **141**, 432–439 (2008).
20. Nagaoka, T. & Uchiyama, A. Development of a small wireless position sensor for medical capsule devices. *Conf. Proc. IEEE Eng. Med. Biol. Soc.* **3**, 2137–2140 (2004).
21. Guo, X., Yan, G. & He, W. A novel method of three-dimensional localization based on a neural network algorithm. *J. Med. Eng. Technol.* **33**, 192–198 (2009).
22. Hashi, S., Yabukami, S., Kanetaka, H., Ishiyama, K. & Arai, K. I. Numerical study on the improvement of detection accuracy for a wireless motion capture system. *IEEE Trans. Magnet.* **45**, 2736–2739 (2009).
23. Hashi, S., Yabukami, S., Kanetaka, H., Ishiyama, K. & Arai, K. I. Wireless magnetic position-sensing system using optimized pickup coils for higher accuracy. *IEEE Trans. Magnet.* **47**, 3542–3545 (2011).
24. Carpi, F., Kastelein, N., Talcott, M. & Pappone, C. Magnetically controllable gastrointestinal steering of video capsules. *IEEE Trans. Biomed. Eng.* **58**, 231–234 (2011).
25. Kuth, R., Reinschke, J. & Rockelein, R. Method for determining the position and orientation of an endoscopy capsule guided through an examination object by using a navigating magnetic field generated by means of a navigation device. German patent US20070038063 (2007).
26. Boese, J., Rahn, N. & Sandkamp, B. Method for determining the position and orientation of an object, especially of a catheter, from two-dimensional X-ray images. German patent US7801342 (2010).
27. Than, T. D. et al. An effective localization method for robotic endoscopic capsules using multiple positron emission markers. *IEEE Trans. Robot.* **30**, 1174–1186 (2014).
28. Dumoulin, C. L., Souza, S. P. & Darrow, R. D. Real-time position monitoring of invasive devices using magnetic resonance. *Magn. Reson. Med.* **29**, 411–415 (1993).
29. Krieger, A. et al. An MRI-compatible robotic system with hybrid tracking for MRI-guided prostate intervention. *IEEE Trans. Biomed. Eng.* **58**, 3049–3060 (2011).
30. Zabow, G., Dodd, S., Moreland, J. & Koretsky, A. Micro-engineered local field control for high-sensitivity multispectral MRI. *Nature* **453**, 1058–1063 (2008).
31. Nagy, Z. et al. in *Proc. IEEE International Conference on Robotics and Automation* 2593–2598 (2009).
32. Gumprecht, J. D. J., Lueth, T. C. & Khamesee, M. B. Navigation of a robotic capsule endoscope with a novel ultrasound tracking system. *Microsyst. Technol.* **19**, 1415–1423 (2013).
33. Wells, P. Current status and future technical advances of ultrasonic imaging. *Eng. Med. Biol. Mag. IEEE* **19**, 14–20 (2000).
34. Carpi, F. & Shaheed, H. Grand challenges in magnetic capsule endoscopy. *Expert Rev. Med. Devices* **10**, 433–436 (2013).
35. Popovic, R. S. *Hall Effect Devices* 2nd edn (CRC Press, Boca Raton, FL, 2003).
36. Saritas, E. U. et al. Magnetic particle imaging (MPI) for NMR and MRI researchers. *J. Magn. Reson.* **229**, 116–126 (2013).
37. Agrawal, D. R. et al. Conformal phased surfaces for wireless powering of bioelectronic microdevices. *Nat. Biomed. Eng.* **1**, 0043 (2017).
38. Agarwal, A. et al. A 4 µW, ADPLL-based implantable amperometric biosensor in 65 µm CMOS. In *2017 Symposia on VLSI Circuits* (2017).
39. Nazari, M. H., Mujeeb-U-Rahman, M. & Scherer, A. An implantable continuous glucose monitoring microsystem in 0.18 µm CMOS. In *2014 Symposium on VLSI Circuits Digest of Technical Papers* 1–2 (2014).
40. Ning, H. et al. Holographic patterning of high-performance on-chip 3D lithium-ion microbatteries. *Proc. Natl Acad. Sci. USA* **112**, 6573–6578 (2015).
41. Liu, T. et al. High-density lithium-ion energy storage utilizing the surface redox reactions in folded graphene films. *Chem. Mater.* **27**, 3291–3298 (2015).
42. Lai, W. et al. Ultrahigh-energy-density microbatteries enabled by new electrode architecture and micropackaging design. *Adv. Mater.* **22**, e139–e144 (2010).
43. Biederman, W. et al. A 4.78 mm² fully-integrated neuromodulation SoC combining 64 acquisition channels with digital compression and simultaneous dual stimulation. *IEEE J. Solid-State Circ.* **50**, 1038–1047 (2015).
44. Monge, M. et al. A fully intraocular high-density self-calibrating epiretinal prosthesis. *IEEE Trans. Biomed. Circuits Syst.* **7**, 747–760 (2013).
45. Ritchie, C. J. et al. Minimum scan speeds for suppression of motion artifacts in CT. *Radiology* **185**, 37–42 (1992).

Author contributions

M.M., M.G.S. and A.E. conceived and planned the research. M.M. designed the integrated circuit and all printed circuit boards, and developed the code to program the FPGA. M.M. performed characterization and in vitro experiments. M.M. and A.L.-G. performed in vivo experiments. M.M. analysed data. M.M., M.G.S. and A.E. wrote the manuscript with input from all other authors. M.G.S. and A.E. supervised the research.

Competing interests

The authors declare no competing financial interests.

Additional information

Supplementary information is available for this paper at doi:10.1038/s41551-017-0129-2.

Reprints and permissions information is available at www.nature.com/reprints.

Correspondence and requests for materials should be addressed to M.G.S. or A.E.

Publisher's note: Springer Nature remains neutral with regard to jurisdictional claims in published maps and institutional affiliations.

nature research

Corresponding author(s):   Mikhail Shapiro, Azita Emami

☐ Initial submission ☒ Revised version ☐ Final submission

Life Sciences Reporting Summary

Nature Research wishes to improve the reproducibility of the work that we publish. This form is intended for publication with all accepted life science papers and provides structure for consistency and transparency in reporting. Every life science submission will use this form; some list items might not apply to an individual manuscript, but all fields must be completed for clarity.

For further information on the points included in this form, see Reporting Life Sciences Research. For further information on Nature Research policies, including our data availability policy, see Authors & Referees and the Editorial Policy Checklist.

▶ Experimental design

1. **Sample size**

   Describe how sample size was determined.

   > Sample sizes were chosen based on preliminary experiments so as to provide sufficient power for statistical comparison (where appropriate).

2. **Data exclusions**

   Describe any data exclusions.

   > No data excluded.

3. **Replication**

   Describe whether the experimental findings were reliably reproduced.

   > All replicates reported in the manuscript.

4. **Randomization**

   Describe how samples/organisms/participants were allocated into experimental groups.

   > n/a

5. **Blinding**

   Describe whether the investigators were blinded to group allocation during data collection and/or analysis.

   > n/a

   Note: all studies involving animals and/or human research participants must disclose whether blinding and randomization were used.

6. **Statistical parameters**

   For all figures and tables that use statistical methods, confirm that the following items are present in relevant figure legends (or in the Methods section if additional space is needed).

n/a	Confirmed	
☐	☒	The exact sample size (n) for each experimental group/condition, given as a discrete number and unit of measurement (animals, litters, cultures, etc.)
☐	☒	A description of how samples were collected, noting whether measurements were taken from distinct samples or whether the same sample was measured repeatedly
☒	☐	A statement indicating how many times each experiment was replicated
☒	☐	The statistical test(s) used and whether they are one- or two-sided (note: only common tests should be described solely by name; more complex techniques should be described in the Methods section)
☒	☐	A description of any assumptions or corrections, such as an adjustment for multiple comparisons
☒	☐	The test results (e.g. P values) given as exact values whenever possible and with confidence intervals noted
☒	☐	A clear description of statistics including central tendency (e.g. median, mean) and variation (e.g. standard deviation, interquartile range)
☐	☒	Clearly defined error bars

See the web collection on statistics for biologists for further resources and guidance.

▶ Software

Policy information about availability of computer code

7. Software

Describe the software used to analyze the data in this study.	n/a

For manuscripts utilizing custom algorithms or software that are central to the paper but not yet described in the published literature, software must be made available to editors and reviewers upon request. We strongly encourage code deposition in a community repository (e.g. GitHub). *Nature Methods* guidance for providing algorithms and software for publication provides further information on this topic.

▶ Materials and reagents

Policy information about availability of materials

8. Materials availability

Indicate whether there are restrictions on availability of unique materials or if these materials are only available for distribution by a for-profit company.	All materials, including circuit designs, available.

9. Antibodies

Describe the antibodies used and how they were validated for use in the system under study (i.e. assay and species).	n/a

10. Eukaryotic cell lines

a. State the source of each eukaryotic cell line used.	n/a
b. Describe the method of cell line authentication used.	n/a
c. Report whether the cell lines were tested for mycoplasma contamination.	n/a
d. If any of the cell lines used are listed in the database of commonly misidentified cell lines maintained by ICLAC, provide a scientific rationale for their use.	n/a

▶ Animals and human research participants

Policy information about studies involving animals; when reporting animal research, follow the ARRIVE guidelines

11. Description of research animals

Provide details on animals and/or animal-derived materials used in the study.	Stated on lines 361-370.

Policy information about studies involving human research participants

12. Description of human research participants

Describe the covariate-relevant population characteristics of the human research participants.	n/a